THE ASTROPHYSICAL JOURNAL, 427:511–518, 1994 May 20

A FABRY-PEROT IMAGER FOR NEAR-INFRARED ASTROPHYSICS AT THE COMMUNICATIONS RESEARCH LABORATORY 1.5 METER TELESCOPE, AND IMAGING OF HYDROGEN RECOMBINATION LINES IN THE ORION NEBULA

HAJIME SUGAI, TOMONORI USUDA, HIROKAZU KATAZA, AND MASUO TANAKA
Institute of Astronomy, University of Tokyo, Mitaka, Tokyo, 181, Japan
HIRONOBU KAWABATA
Tokyo Gakugei University, Koganei, Tokyo 184, Japan
MOTOKO Y. INOUE
Department of Physics, Waseda University, Shinjuku-ku, Tokyo 169, Japan
AND
HIDEKI TAKAMI, TETSUO AOKI, AND NORIHISA HIROMOTO
Communications Research Laboratory, Koganei, Tokyo 184, Japan
Received 1993 April 30; accepted 1993 November 22

ABSTRACT

We have developed a Fabry-Perot imager at the Nasmyth focus of the Communications Research Laboratory (CRL) 1.5 m telescope. The field of view of the camera is 4.'0 × 4.'0, which is the largest among near-infrared Fabry-Perot imagers. In order to make the velocity shift in the field of view small, we chose a long focal length for the collimator (~470 mm). The accurate parallelism of reflecting surfaces, 5 nm, is achieved by systems including a He-Ne laser and Si photodiodes. This gives an effective finesse of ~50. Wavelength calibration is carried out by using a Kr lamp. This calibration includes a correction for wavelength-dependent phase changes in the reflective coatings of the etalon.

Using this Fabry-Perot imager, we obtained Brγ and Paβ images of the Orion Nebula, including the Bright Bar and a part of the Trapezium. From these images we obtained the distributiom of extinction in this area. We found that there are regions with a tendency for the Brγ/Paβ intensity ratio to be larger at a place with a larger Brγ intensity. We conclude that in such regions dust grains exist *within* the ionized region, causing the extinction.

Subject headings: H II regions — instrumentation: interferometers — ISM: individual (Orion Nebula)

1. INTRODUCTION

Fabry-Perot imagers have been used to obtain line images. A Fabry-Perot has a pair of reflecting surfaces facing each other, which is called an etalon. A beam of incident light suffers multiple reflections at the surfaces, and only the light with the wavelength satisfying the condition of interference is transmitted.

Line imaging by a Fabry-Perot imager with a camera has the following advantages over slit-scanning line imagers: (1) they are suitable for morphological studies, (2) the positional accuracy is not sacrificed, and (3) the total flux integrated over the whole region can be evaluated fairly accurately. Moreover, compared with line imaging by a narrow-band filter, the use of a Fabry-Perot imager has advantages: (1) it is possible to obtain continuum-subtracted images more appropriately because of much better spectral resolution, which gives a smaller shot noise from the continuum emission and also enables the subtraction of continuum emission with closer wavelength to line emission, and (2) it is possible to obtain line profiles by scanning the wavelength.

At optical wavelengths, line imaging of Galactic and extragalactic objects has been carried out by using Fabry-Perot imagers such as TAURUS at the Anglo-Australian Telescope (AAT; Taylor & Atherton 1980), HIFI at the University of Hawaii (Cecil, Bland, & Tully 1990), TAURUS-2 at the William Herschel Telescope (WHT; Unger et al. 1990), GFPI at Steward Observatory (Caulet et al. 1992), and CIGALE at ESO (Amram et al. 1992). The recent development of infrared detectors has made it possible to apply the technique to infrared wavelengths. Examples include the Cornell Fabry-Perot interferometer at the Hale Telescope (Herbst et al. 1990), FAST at the Max-Planck-Institut für Extraterrestrische Physik (MPIE) (Rotaciuc et al. 1991), Fabry-Perot at the United Kingdom Infrared Telescope (UKIRT) (Hayashi et al. 1990), and the NRL imaging Fabry-Perot spectrometer at Kitt Peak (Smith & Fischer 1992).

We have been using a near-infrared camera with a field of view of 4.'0 × 4.'0 mounted at the Communications Research Laboratory (CRL) 1.5 m telescope in Tokyo (cf. Aoki 1991). This field of view is larger than a typical value of $\lesssim 1' \times 1'$, and is suitable to cover Galactic objects or nearby galaxies in a single frame (e.g., Sugai et al. 1994). We have developed an imaging Fabry-Perot system for this camera: the Fabry-Perot Imager for Near-Infrared Astrophysics at CRL (FINAC), which is a near-infrared Fabry-Perot imager with the largest field of view yet available. We first describe this system and then show images of the Orion Nebula in hydrogen recombination lines obtained by using this system.

2. OUTLINE OF THE SYSTEM

Figure 1 shows the near-infrared imaging Fabry-Perot on the Nasmyth focus of the CRL 1.5 m telescope. An etalon is set at the position of the image of the secondary mirror. The telescope has a Nasmyth F-ratio of 17.5. Since the main purpose of

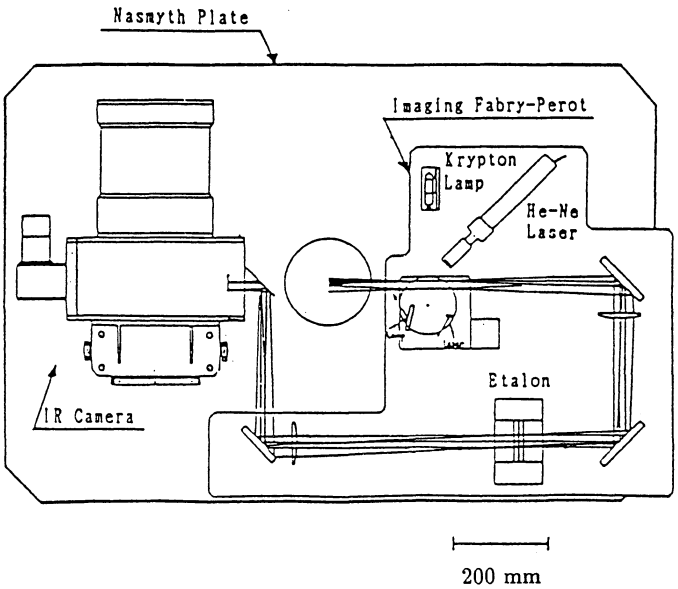

FIG. 1.—Fabry-Perot imager and camera on the Nasmyth plate, which is perpendicular to the altitude axis and can be rotated ±30° from the horizontal position in order to compensate for image rotation. The light reflected by a mirror at the center of the figure, which is inclined 45° to the altitude axis, reaches the infrared camera after passing through the Fabry-Perot. For broad-band imaging the mirror is rotated by 180°.

TABLE 1

CONFIGURATION OF FINAC

Parameter	Value
Telescope: CRL, 1.5 m	
Nasmyth F-ratio	17.5
Detector: Rockwell HgCdTe (1–2.5 μm), 128 × 128 pixel	
Pixel size	60 μm spacing = 1.″88
Quantum efficiency:[a]	
J band	5.9%
H band	13%
K band	20%
Readout noise	700 e^- rms[b]
Gain	340 e^-/DN
Field of view	4.′0 × 4.′0
Fabry-Perot: Etalon, Queensgate Instruments ET85	
Etalon effective area	85 mm
Parallelism of etalon	5 nm
Accuracy of wavelength calibration:	
J band	~10% of velocity resolution
K band	~7% of velocity resolution
Focal length of collimator	470 mm

[a] Including the transmission of a Dewar window and camera lenses.

[b] A net mode, which needs two frames, is used for correcting the time variation of the offset. Therefore, the readout noise for a resultant frame is $\sqrt{2}$ times this value.

this telescope is in research of optical communications, it is not optimized for near-infrared astronomical observations. This causes a large background emission, in particular, at the K band (12.2 mag arcsec^{-2}), probably because of the thermal emission from the telescope and/or the scattered light in the dome (Aoki 1991). Our Fabry-Perot observations, however, are readout-noise–limited. We used a Rockwell HgCdTe 128 × 128 pixel detector with 60 μm pixel size, and a switched MOS-FET TCM-1000B multiplexer. The 4:1 focal reducing optics gives a field of view of 4.′0 × 4.′0 with an image scale of 1.″88 pixel^{-1}. The measured efficiency for the camera system, including a Dewar window, camera lenses, and the quantum efficiency of the array, is 5.9%, 13%, and 20% in the J, H, and K bands, respectively. The readout noise is 700 electrons rms for a frame. Because we use a net mode, in which we obtain a resultant frame by subtracting a short-exposure frame from a long-exposure frame for correcting the time variation of the offset, the resultant readout noise is 1000 electrons.

We have three etalons, with an effective aperture of 85 mm each, made by Queensgate Instruments: J- and K-band etalons of spectral resolution $R \equiv \lambda/\delta\lambda \sim 10^3$, and also a K-band etalon with $R \sim 10^4$. We designed ~95% as the reflectances of the reflecting surfaces. This gives the peak transmission of a Fabry-Perot imager as $\gtrsim$80% when the loss at the reflecting surfaces is $\lesssim$0.5% (e.g., Vaughan 1989; Born & Wolf 1980). This also gives the reflection finesse $N_r \sim 60$. The etalons are piezoelectrically tuned and servo-stabilized by the CS100 controller made by Queensgate Instruments. Three capacitance sensors monitor the parallelism and spacing of an etalon, which are stabilized by feedback signals to piezoelectric actuators. Commands to change the spacing are sent from a personal computer to the CS100 through a standard serial interface.

The Fabry-Perot system includes a He-Ne laser for realizing accurate parallelism of an etalon and also a Kr lamp for wavelength calibration, which are described in § 3 in detail. The configuration of FINAC is summarized in Table 1.

3. CHARACTERISTICS OF THE IMAGING FABRY-PEROT SYSTEM

3.1. *Parallelism of Etalon*

In order to guarantee a large peak transmission and to avoid effects from a nonuniformity of reflecting surfaces on an instrumental line profile, it is desirable to take a defect finesse, N_d, and a parallelism finesse, N_p (e.g., Tanaka et al. 1985), at least about twice as much as a reflection finesse. We have selected $N_r \sim 60$ as described in § 2. Therefore, it is desirable to take $N_d \gtrsim 120$, which is satisfied for our K-band etalons, and also $N_p \gtrsim 120$. We have made systems for accurate parallelism of an etalon to satisfy this condition. For the J band, the system consists of the He-Ne laser (6328 Å) and four Si photodiodes (cf. Tanaka et al. 1985). The laser light, which is expanded and then collimated to cover the whole effective area of the etalon, reaches the Si photodiodes. When we change the spacing of the etalon, the output of the photodiodes on an oscilloscope display changes in an Airy function. We align the etalon so that the phases of four photodiodes' outputs are coincident. Although this system works for the J band, it does not work for the K band because the transmission of the laser light is too small for K-band etalons. For the K band, therefore, we use a laser beam without expanding it. In this system, a laser is set on an X-Y stage so that we can change the point of an etalon where the laser beam passes. We also set a single Si photodiode on another X-Y stage so that the laser beam reaches the photodiode after passing through the etalon. We align the etalon so that the phase of the photodiode's output is coincident at any point of the etalon when we change the spacing of the etalon.

For both J and K bands, we align the output phases of the

photodiode(s) at the accuracy of about a sixtieth order of interference at the wavelength 6328 Å, which means that we have achieved the accuracy of parallelism of 5 nm by using these systems. This accuracy guarantees $N_p \sim 200$ for a J-band etalon and $N_p \sim 400$ for K-band etalons. Without these systems, i.e., realizing only by eye the homogeneity of the collimated laser beam after it passes through an etalon, the accuracy of parallelism could worsen by about an order of magnitude, making a parallelism finesse the most dominant for the effective finesse, i.e., $N_{\rm eff} \sim N_p \sim 30$. The measurement of the effective finesse is shown in § 3.2.

The above systems for an initial accurate parallelism are passive control, i.e., one must stop observations for about 5–10 minutes in order to make the measurement of parallelism. We have found by measurement, however, that the parallelism is extremely highly servo-stabilized by the CS100 controller, giving a stable effective finesse and spectral resolution with only a few percent time variation during a night. Therefore, it is actually enough to measure the parallelism only once a night before observations.

3.2. *Measurements of Etalon Spacing, Order of Interference, and Effective Finesse*

In order to measure the basic parameters of the etalons, such as the spacing, the order of interference, and the effective finesse, a Kr lamp was used in the laboratory. Light from the Kr lamp was collimated to pass through an etalon and focused on an InSb detector with the same light path and F-ratio as in the case of starlight. The spacing of the reflecting surfaces was varied by scanning, and several Kr lines were identified (Table 2). The obtained basic parameters of etalons are shown in Table 3. During observations, the effective finesse and line position are measured by using the near-infrared camera instead of the InSb photometer once every few hours.

3.3. *Wavelength Calibration*

In the identification of Kr lines in § 3.2, we have found that the relative positions of Kr lines are not exactly coincident with the expected ones from the equation of the condition of interference. This is probably caused by phase changes on reflecting surfaces. Phase changes can be treated as contributing to the effective optical spacing of reflecting surfaces (e.g., Vaughan 1989). Figure 2 shows as an example the contribution of phase changes to the effective spacing for the K-band etalon with a velocity resolution of 240 km s^{-1}. The figure clearly shows that the contribution depends on wavelength. In order to set a spacing for an accurate wavelength, we make a correction for phase changes by using this figure. For our etalons, the amount of correction is comparable to the spectral resolution of each etalon, depending on the wavelength of observations and the wavelength of a Kr line used for calibration. The accuracy of the correction corresponds to ~150, 16, and 1.9 km s^{-1} in velocity for the J-band etalon, the K-band etalon with 240 km s^{-1} resolution, and the K-band etalon with 25 km s^{-1} resolution, respectively. The accuracy is high enough for the K-band etalons (~7% of the spectral resolution), while it is not high enough for the J-band etalon (~30% of the spectral resolution). For the J band, therefore, we scan an emission line from a bright object in order to obtain the wavelength at higher accuracy of ~10% of the spectral resolution. The time variation of the peak wavelength, which is caused by a drift of an etalon spacing, is from ~10% up to ~40% of the spectral resolution during a night. We check a wavelength, together with an effective finesse (see § 3.2), once every few hours during observations to keep an accurate wavelength.

TABLE 2

Kr Lines Used for Obtaining Basic Parameters of the K-Band Etalon[a]

Wavelength (μm)	Order
2.0423964	26, 27
2.0446971	26, 27
2.1165471	25, 26
2.1902513	25
2.2485775	24, 25
2.3340416	23, 24
2.3502465	23, 24

[a] With 240 km s^{-1} resolution.

TABLE 3

Basic Parameters of Etalons

Band	Spacing (μm)	Effective Finesse	Order	Velocity Resolution (km s^{-1})
J	~10.3–12.2	~40	~18	~440
K	~26.4–28.3	~50	~25	~240
K	~278.8–280.7	~50	~260	~25

3.4. *Velocity Shift in the Field of View*

In observations using a Fabry-Perot imager, the wavelength with a peak transmission varies over the field of view of the camera. The dependence of the peak wavelength on the

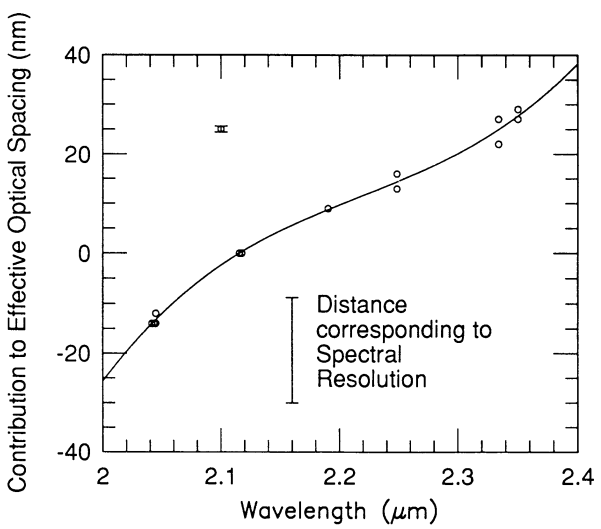

Fig. 2.—Phase changes on reflecting surfaces can be treated as contributing to the effective optical spacing of reflecting surfaces. This figure shows as an example the contribution of phase changes to the effective spacing for a K-band etalon with velocity resolution of 240 km s^{-1}. We define a positive contribution as lengthening the effective spacing. The offset of the contribution is set to zero at the wavelength of one of the Kr lines, 2.1165471 μm. The error bar at the upper left is for the measurements of the contribution of phase changes. The curve is the least-squares fit to a third-order polynomial. In order to set a spacing for an accurate wavelength, we make a correction for phase changes by using this figure.

position in a frame is expressed by the following equation:

$$\Delta v = 1 - \frac{c}{2}\left(\frac{DF}{f}\right)^2 \Theta^2 = -39.6\Theta^2_{\rm arcmin}\ ({\rm km\ s^{-1}})\,, \quad (1)$$

where the diameter D of the telescope is 1500 mm, the F-ratio of the telescope is 17.5, and the focal length f for the collimator is 470 mm. The angular distance Θ is measured from a velocity center, which is set to the frame center. We have chosen a rather long focal length so that the wavelength difference in the frame is small. The actual parabolic coefficient in equation (1) for each etalon was obtained by varying the position of the Kr lamp on an X-Y stage and measuring the peak wavelength for each position. The obtained coefficients, -35 for K-band etalons and -43 for a J-band etalon, were consistent with that expected from equation (1) within the errors of the measurements of the focal length for the collimator, the measurements of the peak wavelengths, and the fitting of a parabolic function. As a result, the wavelength shifts by ~ 160 and ~ 320 km s^{-1} at the edges of the frame and at the corners of the frame, respectively. Except for the K-band etalon with 25 km s^{-1} resolution and also except near the corners of the frame for the lower resolution etalons, this shift is smaller than a spectral resolution element and makes it possible to obtain a line image with one on-line frame with a correction for the spatial variation of line transmission caused by the variation of peak wavelength. We have made a program for such a flux correction assuming that (1) the line width of the observed object is small enough compared with the spectral resolution and (2) the spatial variation of peak wavelength of the line profile is much smaller than the spectral resolution. These assumptions are valid for most Galactic objects. For objects which do not satisfy the assumptions and for the K-band etalon with 25 km s^{-1} resolution, we scan in wavelength to obtain the line profile and the flux. A smaller parabolic coefficient has an advantage also in this case, requiring a smaller number of exposures in order to obtain a set of data with uniform wavelengths over a frame.

3.5. *Transmission*

We calculated the transmission of etalons and that of mirrors and lenses from the measurements of a blackbody and stars. In this calculation we took into consideration the spacing of the reflecting surfaces, and we assumed an Airy function as an instrumental profile. The transmission for the etalons was measured to be $\sim 80\%$, which was consistent with the expected value (see § 2). The transmission for the collimating optics and reimaging optics, including four mirrors and two lenses, was measured to be $\sim 80\%$. Therefore, the total transmission for the Fabry-Perot system is $\sim 60\%$–70%. The transmission for the telescope plus the atmosphere is 20% and 47% for the J and K bands, respectively, and the efficiency for the camera system is 5.9% and 20% for the J and K bands, respectively. We thus obtain the total efficiency, including also the Fabry-Perot system and a narrow-band filter for order sorting (see § 3.6), of 0.58% and 4.3% for the J and K bands, respectively.

3.6. *Order Sorting*

In order to block the light from other orders, we use cooled narrow-band filters (1%) for K-band observations. Now we have three narrow-band filters for Brγ, H_2 $v = 1$–0 $S(1)$ and H_2 $v = 2$–1 $S(1)$, made by Barr Associates. For J-band observations we use a warm narrow-band filter (3%) with a diameter of 50 mm, made by Vacuum Optics Corporation of Japan, and a cold standard J-band filter made by Barr Associates. Warm narrow-band filters, which are set in the collimated beam and close to the etalon, can be tilted in order to adjust the peak transmitted wavelengths to the redshifts of various objects. The relation between the tilt angle and the peak wavelength of narrow-band filters was obtained by using a monochromator in a laboratory. The peak wavelength decreases with an increasing tilt angle, e.g., by 6% at 30° for a 1.312 μm narrow-band filter, corresponding to $\sim 2 \times 10^4$ km s^{-1}. We use the filter with a tilt angle of 17°.5 and 25°.7 for Paβ (1.283 μm) and [Fe II] (1.258 μm), respectively. The transmission does not decrease up to the tilt angle of 40°. The bandwidth also does not change with tilt angle up to 40°, which guarantees the adjacent order rejection.

4. IMAGING OF HYDROGEN RECOMBINATION LINES IN THE ORION NEBULA

4.1. *Spatial Distribution of Extinction from Paβ and Brγ Images*

The extinction for ionized regions is evaluated by using emission lines and/or free-free continuum. The use of hydrogen recombination lines is one of the most reliable methods because the intrinsic line ratios depend almost exclusively on transition probabilities. Optical lines of hydrogen recombination, however, include reflection components (e.g., O'Dell et al. 1992) and make it difficult to derive an accurate value for extinction. Using the near-infrared Fabry-Perot imager FINAC, we observed the central part of the M42 H II region in infrared recombination lines in order to obtain the spatial variation of extinction. The observed area includes the Bright Bar and a part of the Trapezium.

4.2. *Observations and Data Reduction*

The Paβ (1.283 μm) and Brγ (2.166 μm) images were obtained using the Febry-Perot imager we have developed. The summary of the observations is given in Table 4. The data reduction was made using IRAF[1] and also the programs that we made for the Fabry-Perot imaging. At first, the nonlinearity

[1] IRAF is distributed by the National Optical Astronomy Observatories, which is operated by the Association of Universities for Research in Astronomy, Inc. (AURA), under cooperative agreement with the National Science Foundation.

TABLE 4

SUMMARY OF OBSERVATIONS

Characteristic	1992 January 14	1992 February 22
Line	Paβ: 1.283 μm	Brγ: 2.166 μm
Velocity resolution	440 km s^{-1} [a]	240 km s^{-1} [b]
Center velocity	-40, $+1200$ km s^{-1} [c]	-20, $+540$ km s^{-1} [d]
Exposure time/frame	10 minutes	10 minutes
Spatial resolution	6″.9[e]	5″.8[e]

[a] The uncertainty for this observation is several percent.
[b] The uncertainty for this observation is a few percent.
[c] At the center of each frame. The uncertainty is $\sim 10\%$ of the velocity resolution.
[d] At the center of each frame. The uncertainty is several percent of the velocity resolution.
[e] FWHM, including the seeing and the tracking error.

of the sensitivity of the camera was corrected (the quantum efficiency $\eta \propto I^{\alpha}$, where I is the obtained signal and $\alpha \simeq 0.07416 \pm 0.00127$). Next, flat-fielding was carried out using J- and K-band sky frames for Paβ and Brγ images, respectively. We used sky frames not through a Fabry-Perot imager but through a broad-band filter, for the following reasons: (1) The flat field through a Fabry-Perot has the disadvantage of much less signal. In order to restrict the effect of time variation of flat fields to $\lesssim 1\%$, which guarantees discussion in § 4.3, we took a flat field every 1 or 2 hours. This time interval limited the exposure time for a flat field, which was not enough for taking a Fabry-Perot flat field with a shot-noise limited signal-to-noise ratio. (2) We compared a flat field through a Fabry-Perot imager with that through a broad-band filter, which was taken right after the Fabry-Perot flat field, by taking their ratio. We found that the standard deviation of the ratio distribution was 5%. However, for small regions, e.g., of 12 × 12 pixels (see § 4.3), the deviation was very small (<1%) when the contribution from the noise of each frame was taken away. Taking these facts into consideration, we chose to use flat fields through broad-band filters, although they included much broader wavelengths than the Fabry-Perot observations.

Flux calibration was made through the photometry of θ^2 Ori A (O9.5; 4.92 mag at 2.2 μm [Penston 1973] and 5.03 mag at 1.25 μm [Breger, Gehrz, & Hackwell 1981]; its spectrum is assumed to follow the Rayleigh-Jeans law). After flux calibration for each frame, we subtracted an off-line frame from an on-line frame in order to obtain a continuum-subtracted line image. The center velocities of the on-line frame and the off-line frame were $v = -40$ km s^{-1} and $v = +1200$ km s^{-1}, respectively, for Paβ when we define the Hα emission-line velocity, $v_{\rm heliocentric} = 15.5$ km s^{-1} (O'Dell, Wen, & Hester 1991), as $v = 0$ km s^{-1}. The center velocities of the on-line frame and the off-line frame for Brγ were $v = -20$ km s^{-1} and $v = +540$ km s^{-1}, respectively.

In observations using a Fabry-Perot imager, the wavelength with a peak transmission varies over the field of view as discussed in § 3.4. It is possible to carry out a correction for the transmission variation when the line width of the object is small enough compared with the spectral resolution. The spatial variation of the peak wavelength of the object has to be also much smaller than the spectral resolution, a condition which the Orion Nebula satisfies, as do most Galactic objects. The transmission correction, however, causes noise amplification in the outer region, where the transmission is smaller. Therefore, we carried out a correction and restricted discussion to regions where transmission more than half that at the velocity center was secured. In other words, we discuss regions where the wavelength of peak transmission is within half a spectral resolution element from the wavelength at the velocity center, i.e., within $\sim 2'$ radii.

4.3. *Results and Discussion*

Figures 3*a* and 3*b* show the continuum-subtracted images of Paβ and Brγ, respectively. Figure 4 shows the distribution of the Brγ/Paβ intensity ratio. In order to obtain this intensity ratio distribution, we have carried out the following procedures: (1) we selected a region where both line intensities for each pixel are larger than 3 σ; (2) we slightly smoothed the Brγ image by convolving with a Gaussian profile so that its spatial resolution, 5.″8, is reduced to that of the Paβ image, 6.″9; and (3) we took a running mean of 3 × 3 pixels, which roughly corre-

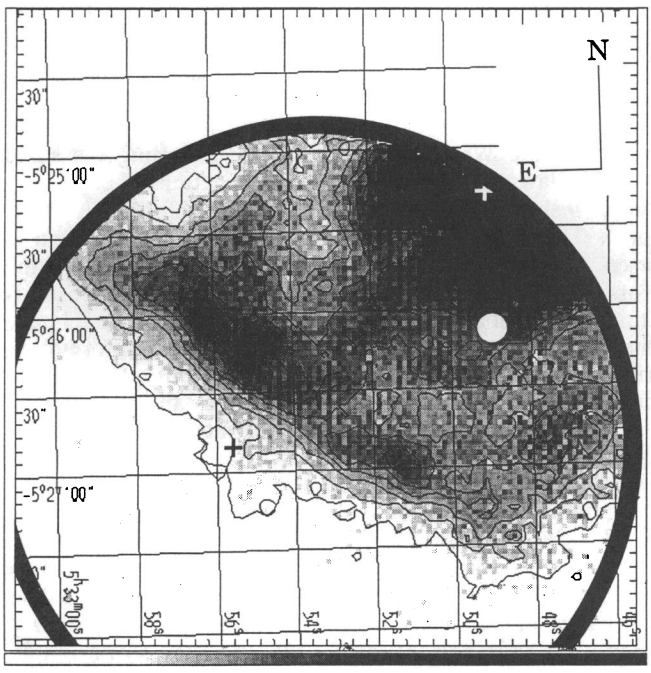

FIG. 3*a*

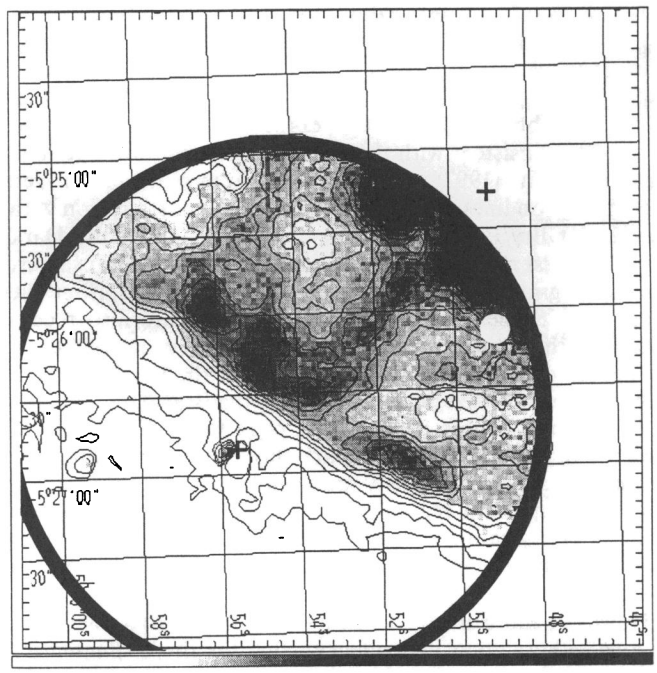

FIG. 3*b*

FIG. 3.—(*a*) Continuum-subtracted line image and contour of Paβ for the Orion Nebula. The lowest contour level and the contour intervals are 3.8×10^{-21} W cm^{-2} arcsec^{-2}, which corresponds to 3 σ for each pixel at the velocity center. The correction for a transmission variation over the field of view was carried out (see text). Only regions are shown where transmission more than half that at the velocity center was secured. Crosses are θ^2 Ori A (*lower left*) and θ^1 Ori C (*upper right*). (*b*) Continuum-subtracted line image and contour of Brγ for the Orion Nebula. The lowest contour level and the contour intervals are 6.4×10^{-22} W cm^{-2} arcsec^{-2}, which corresponds to 3 σ at the velocity center.

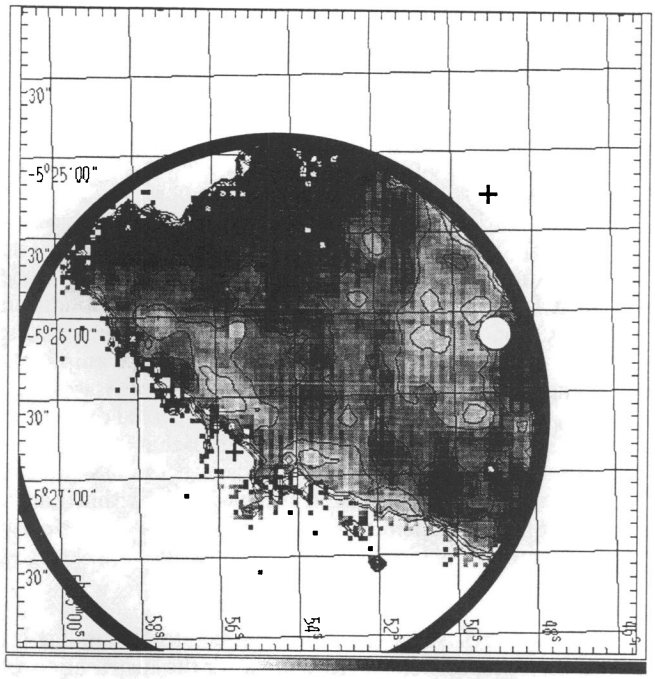

FIG. 4.—Distribution of the Brγ/Paβ intensity ratio with its contour. The contour intervals are 0.025, with the lowest contour level of 0.17, which corresponds to extinction-free. Only regions are shown where both line intensities for each pixel are larger than 3 σ.

sponds to the spatial resolution, for each line image before taking their ratio. We thus took the ratio only for the region selected in step 1. The obtained line ratio varies spatially from ~0.2 to ~0.8, corresponding to almost extinction-free to $A_{Br\gamma} \sim 1.0$ mag if we assume an extinction layer with an extinction law of $\tau_{Br\gamma}/\tau_{Pa\beta} = 2.63$ for the intrinsic line ratio $(I_{Br\gamma}/I_{Pa\beta})_{intrinsic} = 0.17$ (cf. Landini et al. 1984; Osterbrock 1989). The obtained distribution of the Brγ/Paβ intensity ratio is roughly consistent with the extinction distribution obtained by O'Dell et al. (1992) using the line ratio in optical hydrogen recombination lines, Hα/Hβ. In Figure 4, the north region with the largest Brγ/Paβ ratio corresponds to a part of the Dark Bay. The west region with the second largest line ratio is a part of a strong ridge of material extending southwest from the Dark Bay. Some other features in Figure 4 are also recognizable in the extinction distribution by O'Dell et al. (1992).

Figure 5*a* also shows the distribution of the Brγ/Paβ intensity ratio, superposed on the contour of the Brγ image. We find a global tendency for the intensity ratio to be anticorrelated with the Brγ intensity, i.e., the Dark Bay region has a small Brγ intensity and a large intensity ratio, while the Bright Bar region and the Trapezium region have a large Brγ intensity and a small intensity ratio. This implies that the spatial variation of the Brγ intensity is more or less caused by the spatial variation of extinction.

However, more detailed comparison shows that there are regions with an opposite tendency—that the Brγ/Paβ intensity ratio is larger at a place with a larger Brγ intensity. Figure 5*b* shows the relation between the Brγ and Paβ intensities for an example of such regions with a correlation between the Brγ/Paβ intensity ratio and the Brγ intensity. The region includes 12 × 12 pixels (23″ × 23″), and each of 16 data points is the average of a 3 × 3 pixel (5.″6 × 5.″6) area, which is close to the area within the spatial resolution of our reduced images, 6.″9 diameter. Figure 5*c* shows, for comparison, an example of regions with an almost constant Brγ/Paβ ratio. A constant extinction is expressed as a straight line through the origin, with a smaller slope for larger extinction. The data point in Figure 5*c* can be fitted with a straight line of $A_{Br\gamma} \sim 0.29$ mag, with the rms of the residuals, $\sim 9 \times 10^{-22}$ W cm^{-2} arcsec^{-2}, along the vertical axis. This is almost coincident with the combined error of the flux measurements of Paβ and Brγ, $\sim 8 \times 10^{-22}$ W cm^{-2} arcsec^{-2}, where the error for Brγ was transformed into the direction of the vertical axis.

Although it is reasonable to explain a constant Brγ/Paβ intensity ratio in Figure 5*c* by a homogeneous extinction layer outside the ionized region, it is difficult to explain the correlation between the Brγ/Paβ ratio and the Brγ intensity in Figure 5*b* by an extinction layer outside the ionized region. We can show this difficulty by a χ^2 test. Figure 5*b* shows the least-squares fit to a constant extinction model, with a large rms of the residuals, $\sim 1.7 \times 10^{-21}$ W cm^{-2} arcsec^{-2}. When we take a given standard deviation $\sim(8\text{–}9) \times 10^{-22}$ W cm^{-2} arcsec^{-2}, the standard χ^2 value per degree of freedom is 4.2, which rules out a constant-extinction model at a confidence level greater than 99.9%. In order to explain the correlation between the ratio and intensity, we suggest an extinction model by the dust *within* the ionized region. For simplicity, we assume an ionized region with a uniform electron density and uniformly distributed dust. The intensity of a recombination line is expressed by the following equations:

$$I_{Pa\beta,Br\gamma} = (j_{Pa\beta,Br\gamma})_{intrinsic} \int_0^{\tau_0} \exp\left(-\frac{\tau}{\tau_{Pa\beta,Br\gamma}}\right) d\tau$$

$$= (j_{Pa\beta,Br\gamma})_{intrinsic}\, \tau_{Pa\beta,Br\gamma}\left[1 - \exp\left(-\frac{\tau_0}{\tau_{Pa\beta,Br\gamma}}\right)\right], \quad (2)$$

where j is the emission coefficient; $\tau_{Pa\beta}$ and $\tau_{Br\gamma}$ are scale factors for the extinction at the wavelengths of Paβ and Brγ, respectively, in units of optical depth; and τ_0 is the depth of the ionized region. We take $\tau_{Br\gamma} = 2.63\tau_{Pa\beta}$, assuming the same extinction law as that for interstellar extinction. The curve in Figure 5*b* shows the least-squares fit to this intermingled-dust model. The rms of the residuals is $\sim 9 \times 10^{-22}$ W cm^{-2} arcsec^{-2} in the vertical axis, most of which comes from the errors of the flux measurements. Both the fitting to a constant-extinction model and that to an intermingled-dust model have a single fitting parameter. According to Akaike's Information Criterion (Akaike 1973; Aikaike 1977; Sakamoto, Ishiguro, & Kitagawa 1986), therefore, we conclude that an intermingled-dust model is better than a constant-extinction model in this region.

It might be possible to explain the data points in Figure 5*b* by a combination of a homogeneous extinction layer between the H II region and us and an intermingled-dust model. Although it is difficult to discuss this possibility quantitatively because of the uncertainty of the foreground extinction, it does not change our conclusion that the dust within the ionized region plays an important role for the extinction. For example, when we assume the foreground extinction $A_{Br\gamma} \sim 0.1$ mag, the fit of the foreground-extinction–corrected curve to an intermingled-dust model gives a 1.4 times smaller rms of the residuals compared with the case of the fit to a constant-extinction model.

As discussed above, Figures 5*b* and 5*c* show that different

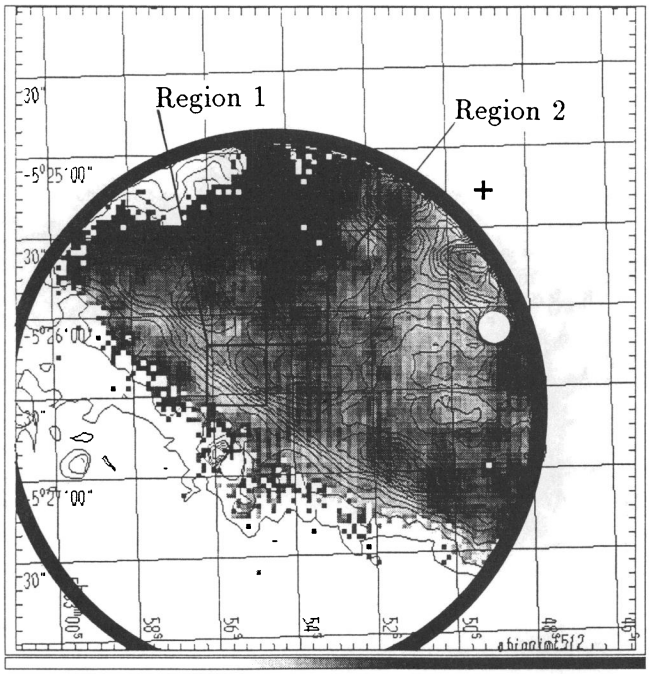

FIG. 5a

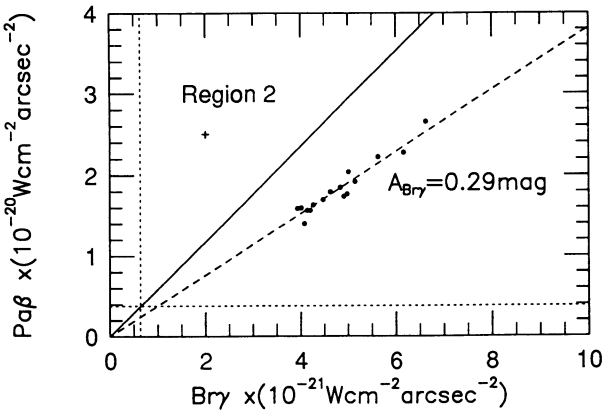

FIG. 5c

FIG. 5.—(*a*) Brγ/Paβ intensity ratio superposed on the contour of the Brγ intensity. (*b*) Relation between the Brγ and Paβ intensities for region 1 in Fig. 5*a*, which includes 12 × 12 pixels (23″ × 23″). Each of the data points is the average of 3 × 3 pixels, and its error bars are shown at the upper left. A constant extinction is expressed as a straight line through the origin, with a smaller slope for a larger extinction. The solid straight line shows the relation for the case of no extinction. The curve is the least-squares fit to an intermingled-dust model, with tick marks for $\tau_0 = 1.0\tau_{Pa\beta}$ and for $\tau_0 = 2.0\tau_{Pa\beta}$, while the dashed lines is the least-squares fit to a constant-extinction model. The dotted lines correspond to 3 σ for each pixel at the velocity center. (*c*) Relation between the Brγ and Paβ intensities for region 2 in Fig. 5*a*. Each of the data points is the average of 3 × 3 pixels, and its error bars are shown at the upper left. The dashed line is the least-squares fit to a constant-extinction model, and it corresponds to a homogeneous extinction layer with $A_{Br\gamma} \sim 0.29$ mag outside the ionized region. The dotted lines correspond to 3 σ for each pixel at the velocity center.

types of extinction play important roles even for close regions: the extinction by a homogeneous layer outside the ionized region for Figure 5*c* and the extinction by dust within the ionized region for Figure 5*b*. Moreover, Figure 5*a* shows that the global tendency of extinction differs from both types of extinction in Figures 5*b* and 5*c*. These facts imply that it is

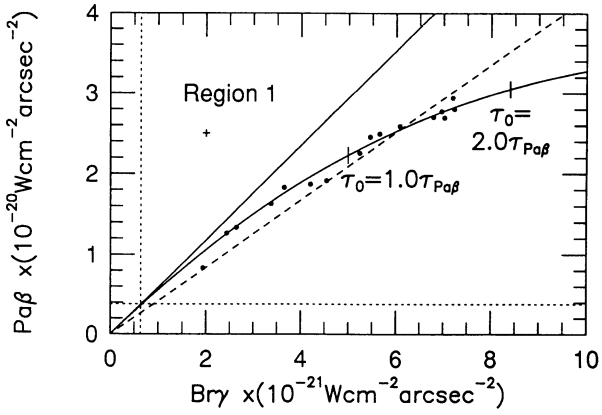

FIG. 5b

essential to obtain imaging data both with a high spatial resolution and with a large field of view in order to understand the extinction of H II regions.

5. SUMMARY

We have developed a Fabry-Perot imager at the Nasmyth focus of the CRL 1.5 m telescope. The characteristics of the system are as follows: (1) The field of view of the camera is 4.′0 × 4.′0. (2) The velocity shift in the field of view is small ($\Delta v = -40\Theta^2_{arcmin}$ km s^{-1}) because we chose a long focal length for the collimator (~470 mm). This enables us to use a large field of view. (3) The accurate parallelism of reflecting surfaces, 5 nm, is achieved by systems including a He-Ne laser and Si photodiodes. The parallelism finesse corresponding to this accuracy is more than 3 times as much as the reflection finesse, which gives an effective finesse of ~50. (4) Wavelength calibration is carried out by using a Kr lamp. This calibration includes a correction for wavelength-dependent phase changes in the reflective coatings of the etalon. (5) The transmission of the etalons was measured to be ~80%, and that of the collimating optics and reimaging optics was also measured to be ~80%. (6) For order sorting we use cooled narrow-band filters for *K*-band observations. A warm narrow-band filter together with a cooled broad-band filter is used for *J*-band observations. Warm narrow-band filters can be tilted in order to adjust the peak wavelengths to the redshifts of various objects, without sacrificing their transmission.

Using this Fabry-Perot imager, we obtained Brγ and Paβ images of the Orion Nebula, including the Bright Bar and a part of the Trapezium. By obtaining the spatial variation of the Brγ/Paβ intensity ratio, we investigated the extinction in this area. In some regions we found that the Brγ/Paβ intensity ratio is constant, which is easily explained by a homogeneous extinction layer outside the ionized region. In some other regions, on the other hand, the Brγ/Paβ intensity ratio is larger at a place with a larger Brγ intensity. We conclude that in such regions dust grains exist *within* the ionized region, causing the extinction.

We would like to thank Masanori Iye for helpful comments. We acknowledge Masaki Sekiguchi for use of a program for data reduction. We also would like to thank the anonymous referee for invaluable comments.

REFERENCES

Akaike, H. 1973, in Second International Symposium on Information Theory, ed. B. N. Petrov & F. Csaki (Budapest: Aladémiai Kiadó), 267
———. 1977, in Application of Statistics, ed. P. R. Krishnaiah (Amsterdam: North-Holland), 27
Amram, P., Marcelin, M., Boulesteix, J., & le Coarer, E. 1992, A&A, 266, 106
Aoki, T. E. 1991, Ph.D. thesis, Univ. Tokyo
Born, M., & Wolf, E. 1980, Principles of Optics (6th ed.; Oxford: Pergamon)
Breger, M., Gehrz, R. D., & Hackwell, J. A. 1981, ApJ, 248, 963
Caulet, A. Woodgate, B. E., Brown, L. W., Gull, T. R., Hintzen, P., Lowenthal, J. D., Oliversen, R. J., & Ziegler, M. M. 1992, ApJ, 388, 301
Cecil, G., Bland, J., & Tully, R. B. 1990, ApJ, 355, 70
Hayashi, S. S., Hasegawa, T., Tanaka, M., Hayashi, M., Aspin, C., McLean, I. S., Brand, P. W. J. L., & Gatley, I. 1990, ApJ, 354, 242
Herbst, T. M., Graham, J. R., Beckwith, S., Tsutsui, K., Soifer, B. T., & Matthews, K. 1990, AJ, 99, 1773
Landini, M., Natta, A., Oliva, E., Salinari, P., Moorwood, A. F. M. 1984, A&A, 134, 284
O'Dell, C. R., Walter, D. K., & Dufour, R. J. 1992, ApJ, 399, L67
O'Dell, C. R., Wen, Z., & Hester, J. J. 1991, PASP, 103, 824
Osterbrock, D. E. 1989, Astrophysics of Gaseous Nebulae and Active Galactic Nuclei (Mill Valley: University Science Books)
Penston, M. V. 1973, ApJ, 183, 505
Rotaciuc, V., Krabbe, A., Cameron, M., Drapatz, S., Genzel, R., Sternberg, A., & Storey, J. W. V. 1991, ApJ, 370, L23
Sakamoto, Y., Ishiguro, M., & Kitagawa, G. 1986, Akaike Information Criterion Statistics (Tokyo: KTK Scientific Publishers)
Smith, H. A., & Fisher, J. 1992, ApJ, 398, L99
Sugai, H., et al. 1994, ApJ, 420, 746
Tanaka, M., Yamashita, T., Sato, S., & Okuda, H. 1985, PASP, 97, 1020
Taylor, K., & Atherton, P. D. 1980, MNRAS, 191, 675
Unger, S. W., Taylor, K., Pedlar, A., Ghataure, H. S., Penston, M. V., & Robinson, A. 1990, MNRAS, 242, 33P
Vaughan, J. M. 1989, The Fabry-Perot Interferometer (Bristol and Philadelphia: Adam Hilger)